Roy *et al. Advances in Bridge Engineering* (2022) 3:18
https://doi.org/10.1186/s43251-022-00065-y

Advances in
Bridge Engineering

ORIGINAL INNOVATION Open Access

Investigation of the performance of grouted couplers in vehicle impacted reinforced concrete ABC bridge piers

Suman Roy*, Ikwulono D. Unobe and Andrew D. Sorensen

*Correspondence:
sumanroy74@gmail.com

Department of Civil
and Environmental Engineering,
Utah State University, Logan, UT
84322, USA

Abstract

Increased dynamic impact on bridge piers caused by seismic events, blasts, and vehicular impact have become increasingly common. Recent research efforts indicate that code provisions for designing reinforced concrete members to withstand such dynamic loads are inadequate and need additional insights for this purpose. Numerous works have been undertaken to investigate reinforced concrete (RC) traditional bridge pier performance on high strain rate loading. However, little attention has been given to evaluate the performance of connections used in present day bridges including accelerated bridge constructions (ABC) to withstand vehicle impacts, and hence, is relatively unknown. In this study, the use of grouted couplers to contain the unbalanced moments resulting from vehicular impact forces exceeding the moment capacity of the reinforced concrete piers and avoiding extensive damage to the piers is investigated. A representative column, typical of those specified by state departments of transportation, is studied to determine the performance. The performance of the coupler is investigated for both dynamic and static combined stresses. Quasi-static to dynamic strain rates of steel reinforcement connected to the couplers is also evaluated. Quantifying the stresses and strains developed at coupler region from dynamic impact can help coupler manufacturers to optimize the strength properties, thus improving serviceability. This study investigated utilizing splice sleeves in mitigating the formation of plastic hinges, as well as addressing the essential properties of coupler sections required to adequately carry out this function, and will provide a useful design tool for the manufacturers, forensic structural engineers, and practitioners.

Keywords: Grouted coupler, Splice sleeve, Bridge pier, Unbalanced moments, Impact, Strain

1 Introduction

Bridge piers experience highly dynamic loading due to a variety of loading conditions including seismic events, blast events, and vehicular collisions. This may cause health deterioration of the column ranging from cosmetic damage to collapse. The other mechanisms comprising of dynamic impact loads (vehicular collisions and blast) have received more attention for traditional RC bridge piers. However, the performance of connections used in present day bridges including accelerated bridge constructions

Springer Open

© The Author(s) 2022. **Open Access** This article is licensed under a Creative Commons Attribution 4.0 International License, which permits use, sharing, adaptation, distribution and reproduction in any medium or format, as long as you give appropriate credit to the original author(s) and the source, provide a link to the Creative Commons licence, and indicate if changes were made. The images or other third party material in this article are included in the article's Creative Commons licence, unless indicated otherwise in a credit line to the material. If material is not included in the article's Creative Commons licence and your intended use is not permitted by statutory regulation or exceeds the permitted use, you will need to obtain permission directly from the copyright holder. To view a copy of this licence, visit http://creativecommons.org/licenses/by/4.0/.

(ABC) to withstand high strain rate loading from vehicle impacts is relatively unknown. Despite different studies showing that vehicular collisions with bridge elements are the most common dynamic impact scenario, especially with the increasing volumes of vehicular traffic (Sharma et al. 2015). As such, it is imperative to investigate the response of reinforced concrete bridge (RC) piers to vehicle collisions and also possible methods of enhancing the capacity of the piers to withstand such events.

Investigations into the failure mechanisms of bridge piers subjected to vehicular impact have shown that the failure of these members will primarily occur from excessive shear as well as overturning moments occurring at the column base (El-Tawil et al. 2005; Thilakarathna et al. 2010). Recent studies of the structural reliability of RC columns subjected to sequential loading of blast and vehicular impact have shown that the structural reliability of the columns are particularly sensitive to the shear reinforcement, column diameter, and reinforcement ratio (Thomas et al. 2018; Roy et al. 2022). This implies that an increase in the stiffness of the column could possibly help it withstand the external forces caused by vehicular impact. Traditional pier sections have been studied as a means of increasing the stiffness of reinforced concrete (RC) columns to improve their seismic performance, energy dissipation (Roy and Sorensen 2021a), failure mechanism in terms of crack propagation (Roy and Sorensen 2021b), and to overcome the development of plastic hinges (Ebrahimpour et al. 2016; Girão Coelho et al. 2012; Pantelides et al. 2014; Tazarv and Saiidi 2016). The failure mechanism of the grouted coupler at the post behavior from vehicle impact at high strain rate loading has been presented in this study. However, the effect of these couplers performance on the response of these piers to vehicle impact is still relatively unknown, and hence needs an additional scrutiny.

This study presents the grouted coupler section undergoing short duration vehicle impact load to predict the coupler behavior, material properties and post impact performance as well. Splice-sleeve along with high grade concrete grouted coupler are placed where plastic hinges are highly expected to form (Ebrahimpour et al. 2016), particularly at the pier and pier-foundation junction. Performance of the pier and the dynamic impact on it are studied for axially compressive stress, and the combined stresses as a result of residual flexure due to impact at column base for individual coupler. However, precise assessment of the performance of splice-sleeve along with grouted coupler used in ABC needs deeper attention to be carried out (Ameli et al. 2016).

To analyze the impact characteristics of grouted coupler, it is placed in the pier- foundation connection in order to evaluate the performance standard of the splice sleeve and grouted coupler mechanism as a composite material (Jacob et al. 2004). Coupler sections have been studied as a means of increasing the stiffness of the RC piers to improve their seismic performance and overcome the development of plastic hinges (Tazarv and Saiidi 2016; Thomas et al. 2018). In the present study, splice-sleeves along with high grade concrete grouted coupler are embedded into the pier-foundation, placing the foundation top and the coupler cross-section in the same level. As such, failure mechanism of each coupler along with the material properties need rigorous prior investigation before recommending its widespread use in foundation-pier connection for ABC under axially compressive stress, and the combined stresses resulting from residual flexure caused by impact load, transferring it at pier base (Zhou et al. 2017).

The importance of this holistic study is to examine static and dynamic characteristics of the single grouted coupler material used in RC ABC bridge pier to withstand short duration vehicle impact. In order to assess post impact behavior and enhancing the performance level, study of coupler on dynamic load requires additional scrutiny. In addition, to determine the stress-strain relationship of the coupler region and to directly capture stress and strain levels, some physical properties of the coupler system are studied comprising from uniaxial stress and strain system by utilizing the rebar stress and strain level.

2 Representative reinforced concrete (RC) pier

In this study, a representative circular reinforced concrete (RC) pier section is considered (as shown in Fig. 1). The concrete in the pier is specified to have a compressive strength of 3 ksi (20.68 MPa) and the reinforcing steel a yield strength of 60 ksi (413.68 MPa). The unrestrained length of the pier is taken as 8.6 ft (2.62 m) with circular cross-section throughout (Grouted splice sleeve connectors for ABC bridge joints in high-seismic regions – transportation blog n.d.) as shown in Fig. 1.The outer diameter and the inner diameter (h) of the concrete column are 21 in. and 18 in., respectively. The pier has primary reinforcement of 6 no. 8 ASTM 706 Grade 60 steel reinforcing-bars and shear reinforcement of # 4 steel rebars at $2\frac{1}{2}$ inches center to center (pitch) spirally conforming to the ACI minimum shear reinforcement criteria (ACI 2011). In addition, the representative pier also satisfies the shear reinforcement criteria for rebar diameter, and pitch of the spiral reinforcement (Furlong 2014).

3 Nominal moment strength (M_N) of reinforced concrete pier

Material and sectional details of the representative test column used in determining the nominal moment capacity are shown in Table 1.

The detailed cross section with stress block diagram of the pier is further shown in Fig. 2. As per ACI specifications, a balanced strain condition is considered to exist at a cross-section where the tension steel reaches the strain corresponding to the yield

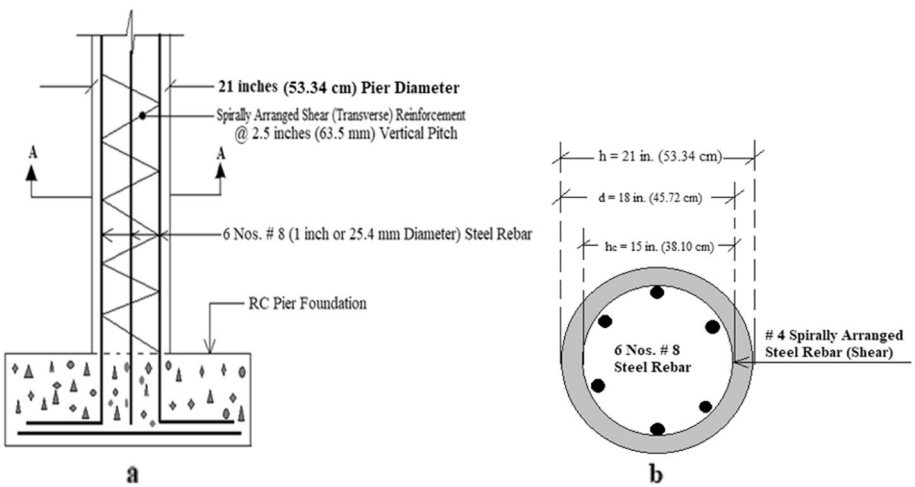

Fig. 1 **a** Representative RC bridge pier, **b** Section A-A

Table 1 Representative test pier details

Compressive Strength of Concrete (f'_c) (psi) (MPa)	3000 (20.68)
Yield Strength of Longitudinal Steel (psi) (MPa)	60,000 (413.68)
Modulus of Elasticity (concrete) (psi) (MPa)	3.12×10^6 (21,511.64)
Modulus of Elasticity (steel) (psi) (MPa)	20×10^6 (1.38×10^4)
β_1	0.85
Modular Ratio (n) (E_s / E_c)	9.295
Diameter of Column (in.) (cm)	21 (53.34)
Concrete Cover (in.) (cm)	1.5 (38.1)
Diameter of Longitudinal Steel (in.) (cm)	1 (25.4)
Diameter of Transverse Steel (in.) (cm)	0.5 (12.7)
Height of Column (in.) (m)	102 (2.6)

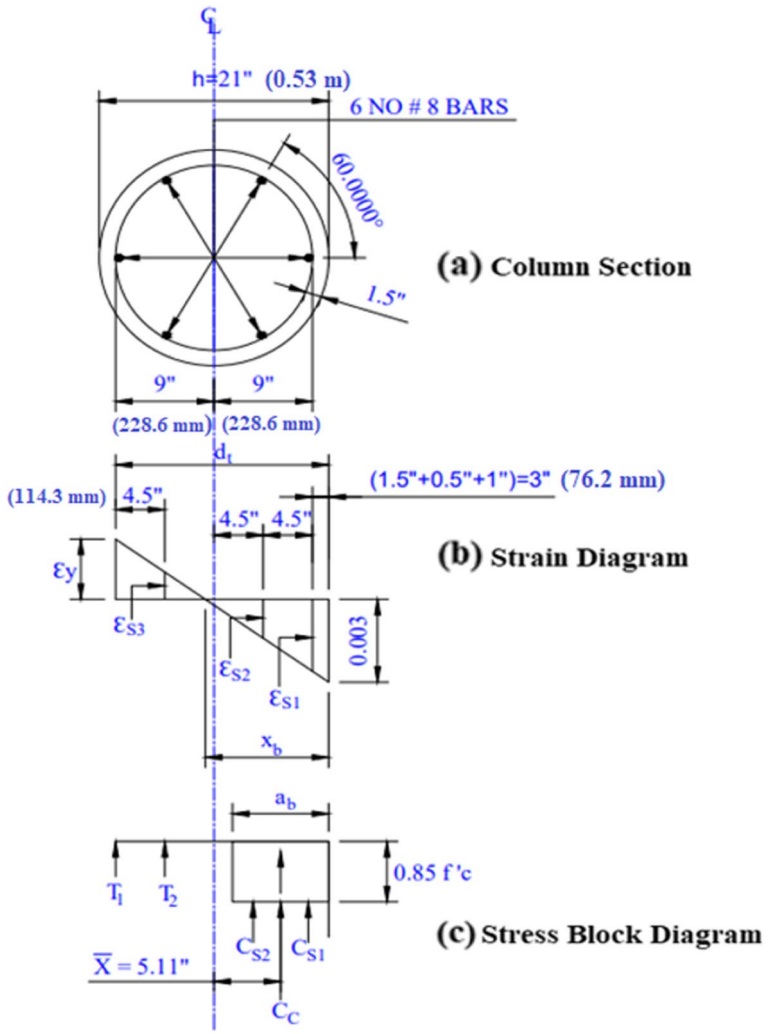

Fig. 2 Column section with strain and stress block diagram

strength of the steel (f_y) as the concrete crushing strain reaches its maximum value of 0.003. Thus, strain ε_y here, is determined as the yield strain of steel i.e. 0.00206 (f_y / E_s) (ACI 2011).

To determine the nominal moment capacity of the reinforced concrete section, a procedure as laid out by Hsiao is followed (Hsiao 2012). First, the distance of the extreme compression fiber to the neutral axis of the section is determined as shown in Eq. 1 (MacGregor et al. 2012).

$$x_b = \frac{0.003}{0.003 + \varepsilon y}(d_t) \tag{1}$$

Where: d_t is the distance from the extreme compression fiber to the extreme tension steel and calculated as; $d_t = h - cover - diameter\ of\ main\ bar - diameter\ of\ stirrup\ bar$, and ε_y is the yield strain of the reinforcing steel.

The depth of the 'Whitney' equivalent rectangular stress distribution in concrete for the balanced strain condition is then determined using Eq. 2.

$$a_b = \beta_1(x_b) \tag{2}$$

Where: β_1 is 0.85 for $f'_c \leq 4000$ psi (27,579.03 kN/m^2) (ACI 2011).

The properties of circular compression block including its gross concrete area and centroid are then computed and as shown in the Eqs. 3 to 5 (Hsiao 2012).

$$\alpha = \cos^{-1}\left\{\frac{(h/2 - a_b)}{h/2}\right\} \tag{3}$$

$$A_{cb} = \frac{h^2}{2}\left(\frac{\alpha}{2} - \frac{1}{4}\sin 2\alpha\right) \tag{4}$$

$$\overline{X} = \frac{\left[\frac{h^3}{4}\left(\frac{\sin^3\alpha}{3}\right)\right]}{A_{cb}} \tag{5}$$

Where: h is the diameter of the column, a_b is the depth of the 'Whitney' block as determined in Eq. 2, A_{cb} is the area of the circular compression block and $\overline{X}$ is the centroid location of the compression concrete block.

The computed area of the compression block is next used to determine the compression force in concrete for circular compression block, C_c, as shown in Eq. 6 (MacGregor et al. 2012).

$$C_c = 0.85 f'_c A_{cb} \tag{6}$$

3.1 Computation of the strains, and forces in tension and compression steel

Referring to Fig. 2 and from the geometry of similar triangles, strains in different fibers (ε_{s1}, ε_{s2}, and ε_{s3}) are computed, and using the computed values the forces in the steel (T_1, T_2, C_{s1} and C_{s2}) are determined as, $T_1 = A_s\ f_y$, $T_2 = A_s\ ^*E_s{}^*\varepsilon_{s3}$, $C_{s1} = A_s\ (f_y - 0.85^*f'_c)$, and $C_{s2} = A_s\ (\varepsilon_{s2}{}^*\ E_s - 0.85f'_c)$.

The computed parameters are then used in calculating the nominal moment capacity ($M_{n,g}$) for the gross concrete area of the column (Fig. 1) as shown in Eq. 7 (Hsiao 2012).

$$M_{n,g} = C_c\overline{X} + (T_1 + C_{s1})\left(d_t - {}^{h}/_{2}\right) + (T_2 + C_{s2})\left(d_t - {}^{h}/_{2}\right)/2 \tag{7}$$

From Eq. 7 and the specifications of the representative RC bridge pier, nominal strength of RC concrete for gross cross-sectional area of column was computed as 3143.3236 kip-in (385.65 kN-m).

A similar process is used to estimate the nominal moment capacity of the core area of the column. Core concrete is confined by the laterally placed spiral tie to prevent lateral expansion due to Poisson's ratio, and incurs the axially compressed overloading due to impact. Confined concrete can enhance the performance in terms of capacity and deformability due to stress compatibility. The confinement of the core concrete contributes in improving ductility and after peak-stress deformability in addition to increasing the axial load carrying capacity (Karim et al. 2014). The nominal core area capacity, computed using the reduced cross-sectional area is determined to be 2007.206 kip-in (226.78 kN-m).

4 Determination of dynamic flexure

This study investigates sections of the vehicular impact scenario on reinforced concrete sections. A semi-trailer is considered as the vehicle for the impact event as this represents a worse-case scenario. Vehicle weight and impact velocity of the semi-trailer are considered as 80,000 lbs. (355.86 kN) and 100 ft./sec (30.48 m/sec) respectively to simulate a fully loaded trailer condition moving at its allowed speeds on the highway (Speeding and speed limits index and overview n.d.).

As a result of the parameters selected in this investigation, the vehicular impact scenario being studied is of the high-velocity, low duration variety. This will result in a high strain rate of loading for both the concrete and steel components of the RC pier. Concrete and steel both manifest a peculiar phenomenon when placed under such high loading rates (Auyeung et al. 2019). This phenomenon is an observable increase in strength capacity of these materials, as a function of the strain rate effect on reinforced concrete. As a result, a dynamic impact factor was proposed by (Malvar 1998), to reflect this increase on the strength capacity parameters of the reinforced concrete member.

4.1 Determination of dynamic increase factor (DIF)

Determination of the dynamic increase factor (DIF) reflecting the material behavior of concrete and steel during a vehicular impact scenario, involves an estimation of the dynamic flow stress from the impact. This dynamic flow stress can be estimated for either material. The dynamic flow stress (σ_{dyn}) in steel at impact is selected for use as it is projected to be the critical component of the member with respect to the coupler section. This dynamic flow stress is determined using Eq. 8 (Feyerabend 1988).

$$\sigma_{dyn} = \sigma_y \left[1 + \left(\frac{\dot{\varepsilon}}{C}\right)^{\frac{1}{p}}\right] \tag{8}$$

Where: σ_y is a static flow stress and is considered as 60 ksi (420 MPa) for ASTM 706 Grade 60 steel rebar, C and p are the material constants (Cowper and Symonds 1957;

Zhou and Li 2018) with values of 40 and 5 [8] respectively. Quasi-static strain rate of steel re-bar ($\acute{\varepsilon}$) is considered as $0.16\,\mathrm{sec}^{-1}$ for impacting velocity 100 ft./sec (30.48 m/sec) (Cowper and Symonds 1957).

The dynamic parameter 'ξ' can be computed from Eq. 9 (Malvar and Crawford 1998; Mander et al. 1988) and Eq. 8.

$$\xi = 0.019 - 0.009\left(\frac{\sigma_{dyn}}{60}\right) \tag{9}$$

Where: ξ is a constant which depends on the dynamic yield stress of steel at the strain hardening zone, $\acute{\varepsilon}$ is the strain rate of steel and σ_{dyn} is the dynamic flow stress at uni-axial plastic strain rate of steel.

The DIF can be computed from Eq. 10 (Malvar and Crawford 1998; Mander et al. 1988), using Eq. 9.

$$DIF = \left(\frac{\acute{\varepsilon}}{10^{-4}}\right)^{\xi} \tag{10}$$

Replacing the value of ξ from Eq. 9 to Eq. 10, yields a DIF of 1.053.

4.2 Computation of static force at impact

The time dependent frontal shock from vehicular impact can be computed using an averaged integration of the instantaneous impact force over the range of 50 ms near the peak impact force as shown in Eq. 11 (Zhou and Li 2018).

$$I_{dyn} = \frac{\int_{t_d-0.025}^{t_d+0.025} I_r \sin\left(\frac{\pi t_d^{+}}{t}\right) di}{0.05} \tag{11}$$

Where: I_{dyn} represents the frontal shock due to impact, $I_{r,}$ is the peak reflected pressure (overpressure), $t_d{}^{+}$ is the time instant of the peak impact force, and t represents the impact duration.

Developed to estimate the total static force of a vehicle impact from the instantaneous peak force occurring during impact, the relationship shown in Eq. 11 captures the expected loading history of the impact over time on the RC pier (Zhou et al. 2017) utilizing the expected sinusoidal loading pattern of the impact event to predict the dynamic load from the peak force and the loading time history.

The overpressure represented by $I_{r,}$ is a function of the kinetic energy (E) from the impacting vehicle and can be determined using Eq. 12, Eq. 12 was developed as a relationship between bending stress developed in the pier from the peak dynamic force of impact and kinetic energy using data from various simulated and experimental studies (Cao et al. 2019; Gomez and Alipour 2014; Mohammed and Parvin 2013; Zhou and Li 2018). The bending stress was used in lieu of the impact force so as to capture the possible effects of geometric variations of the pier in the resulting overpressure from regression analysis at impact as shown in Eq. 12 (Roy et al. 2021). Boundary conditions of the pier is considered as bottom end fixed and top end restrained from displacement and rotation (Zhang et al. 2018) is as shown in Fig. 4c.

$$I_r = \left(4 \times 10^{-5} E\right) * \frac{4I}{(L.c)} \tag{12}$$

Where: E is the kinetic energy, absorbed by the impacted pier, I is the moment of inertia of the pier section, L is the height of the pier and c is the perpendicular distance from the neutral axis of the cross section to the farthest point on the cross section of the pier, as shown in Fig. 3.

Assuming the vehicle comes to rest without rebounding from the pier, the kinetic energy (E) equation is determined as same as the kinetic energy (E) of the vehicle using Eq. 13 (Tsang and Lam 2008).

$$E = 0.5 M_{veh} V^2 \tag{13}$$

Where: E is impact energy of the vehicle, M_{veh} represents the weight of the impacting vehicle, and V is the frontal impact velocity of the vehicle causing instability of the column.

4.3 Computation of external flexural moments

Moments caused by the lateral impact force from vehicle collisions are induced at the base of the column as well as at different levels between the point of impact and the base. These moments if exceeding the moment capacity of the column could result in structural failure.

Assuming a pinned connection for the RC column, the static moment (M_s) induced by the vehicular collision can be determined as shown in Eq. 14.

$$M_s = I_{dyn} * H \tag{14}$$

Where: H is the height (in feet) to compute static moment and I_{dyn} represents the frontal shock due to impact.

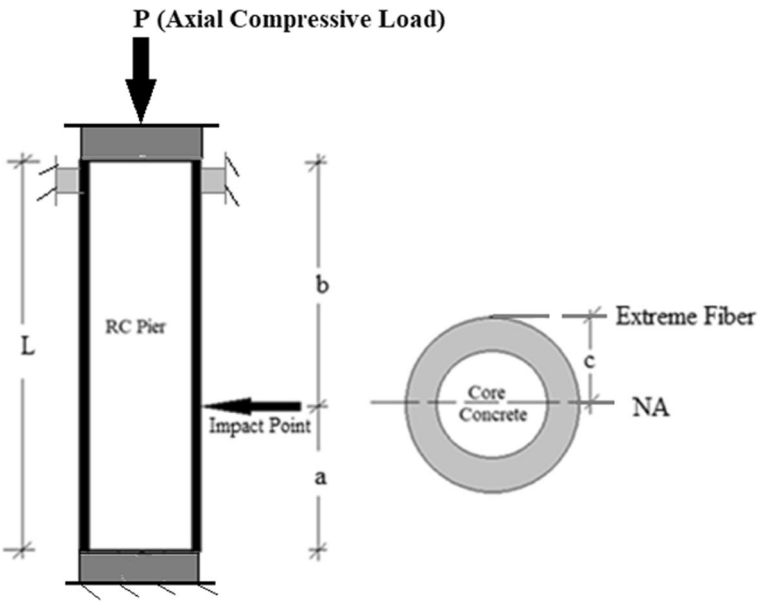

Fig. 3 Impact Location and Geometry of RC Bridge Pier (Roy et al. 2022)

4.3.1 Dynamic moment

Dynamic moments (M_{dyn}) to investigate flexural effects at different fibers have been determined by static moment (M_s) times the dynamic increase factor (DIF). This is further expressed in Eq. 15 as to investigate the increased flexural effect (Feyerabend 1988).

$$M_{dyn} = DIF * M_s \tag{15}$$

Where: DIF is the dynamic impact factor and M_s is the static moment.

4.4 Unbalanced moments from static and dynamic impact

Unbalanced moments in the column are caused by the exceedance of the moment capacity of the column and by the moments induced by the impact force. These unbalanced moments can be resisted by the splice-sleeve and grouted coupler system formed by the six couplers (six reinforcing steel bars are embedded into grout), one at the base of each longitudinal reinforcement as shown in the Fig. 4a. Determined as external static moments at column base for gross and core cross-sectional area minus sectional moments of resistance at gross and core cross-sectional areas, unbalanced static and dynamic moments for both gross and core cross-sectional areas are computed as shown in Eqs. 19 through 22. Figure 4a and b show the coupler arrangement in a column base embedded into the footing. Boundary conditions (fix-fix ended at bottom and top end is restrained from displacement and rotation) are shown in Fig. 4c. Computations of unbalanced moments are computed while semi-trailer impacts occur due collision at different heights in column has been further shown in Fig. 8.

4.4.1 Unbalanced static moment for gross cross-sectional area

Static unbalanced moment ($M_{un,sg}$) for gross cross-sectional area has been computed in Eq. 16, as,

$$M_{un,sg} = M_{s,g} - M_{n,g} \tag{16}$$

Where: $M_{s,g}$ is the external static moment for gross cross-sectional area.

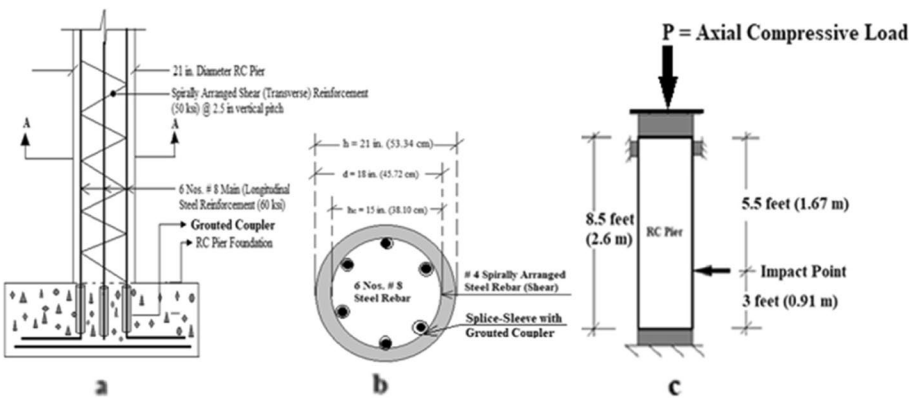

Fig. 4 Schematic diagram of coupler arrangement in **a** pier-foundation, **b** section A-A and **c** boundary conditions and loading type

4.4.2 Unbalanced static moment for core concrete area

Static unbalanced moment ($M_{un,sc}$) for core cross-sectional area has been computed in Eq. 17, as,

$$M_{un,sc} = M_{s,c} - M_{n,c} \tag{17}$$

Where: $M_{s,c}$ is the external static moment at core cross-sectional area of concrete column.

4.4.3 Unbalanced dynamic moment for gross concrete area

Dynamic unbalanced moment ($M_{un,dg}$) for core cross-sectional area has been computed in Eq. 18, as,

$$M_{un,dg} = M_{dyn,g} - M_{n,g} \tag{18}$$

Where: $M_{dyn,g}$ is the dynamic moment caused due to dynamic impact at gross cross-sectional area of concrete pier.

4.4.4 Unbalanced dynamic moment for core concrete area

Dynamic unbalanced moment ($M_{un,dc}$) for core cross-sectional area has been computed in Eq. 19, and as shown in Fig. 5.

$$M_{un,dc} = M_{dyn,c} - M_{n,c} \tag{19}$$

Where: $M_{dyn,c}$ is the dynamic moment caused due to impact at core cross-sectional area of concrete.

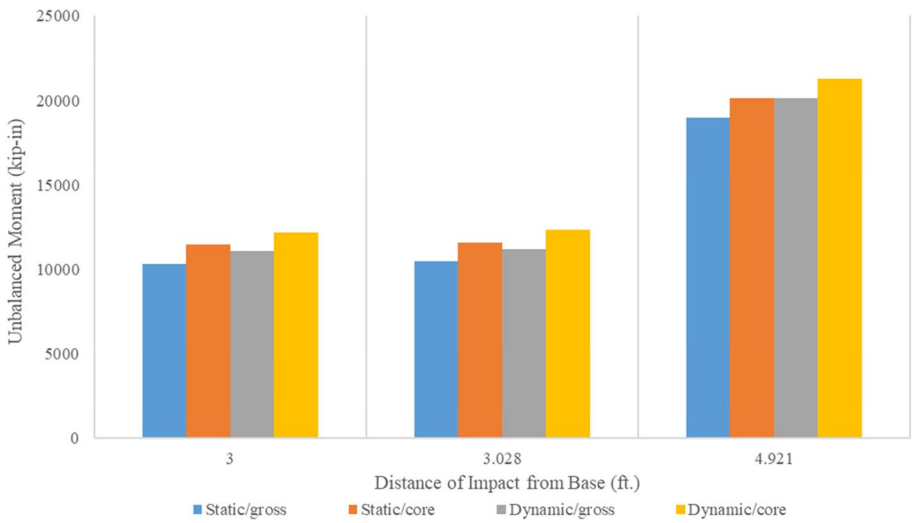

Fig. 5 Unbalanced moments at pier base while impact at different heights in pier

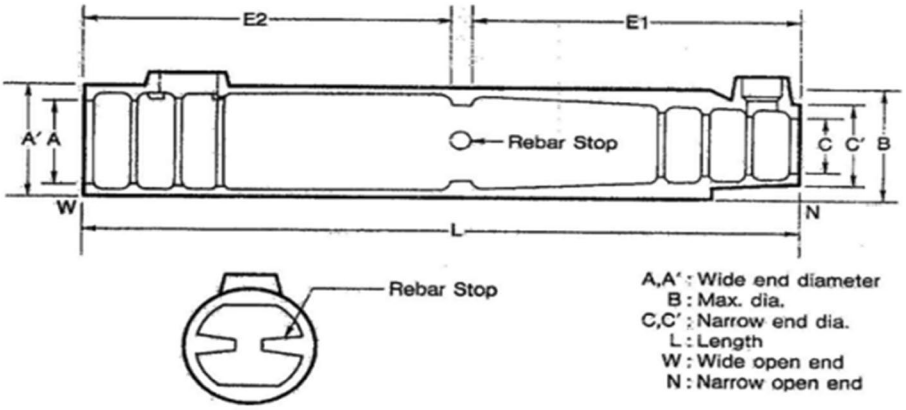

Fig. 6 Splice sleeve specifications as per NMB General Brochure (ICC-ES Evaluation Report ESR-3433 2014)

Table 2 Details of splice sleeve number 8 U-X (ICC-ES Report 2016)

Position	Coupler Type	Internal Diameter (in) (mm)	External Diameter (in) (mm)
W = Wider end	8 U-X	1.89 (48.01)	2.52 (64.01)
N = narrower end	8 U-X	1.3 (33.02)	2.52 (64.01)

5 Coupler detail to withstand unbalanced moments

Splice-sleeve used for grouted coupler in the column rebar properly embedded and placed (Fig. 4) appreciably predicts better performance in dynamic response. Grouted couplers are embedded in the foundation to act as a rigid body and in conjunction with the foundation, attract the maximum impact force. Foundations are rigid bodies and are less slender than piers. So a coupler embedded in the foundation is expected to perform better than if embedded in the pier (Pantelides et al. 2014). For this particular study, the splice sleeve detail recommended as per 'Splice Sleeve North America' and 'NMB General Brochure' (ICC-ES Evaluation Report ESR-3433 2014) are considered and shown in Fig. 6.

For this particular study, sleeve number 8 U-X (ICC-ES Report 2016) has been selected for the # 8 ASTM 706 (ASTM 2015) bars used in column for main reinforcement. Splice-sleeve (ICC-ES Report 2016) details used in this study are tabulated and shown in Table 2.

Various connection types have been studied for precast concrete bridge columns in seismic areas in two major categories of emulative and rocking connections (Girão Coelho et al. 2012). The emulative connection for precast components is defined as a connection that incorporates special details resulting in a performance that emulates that of a monolithic cast-in-place component as shown in the Fig. 7. The steel rebar becomes discontinuous at the middle of splice sleeve.

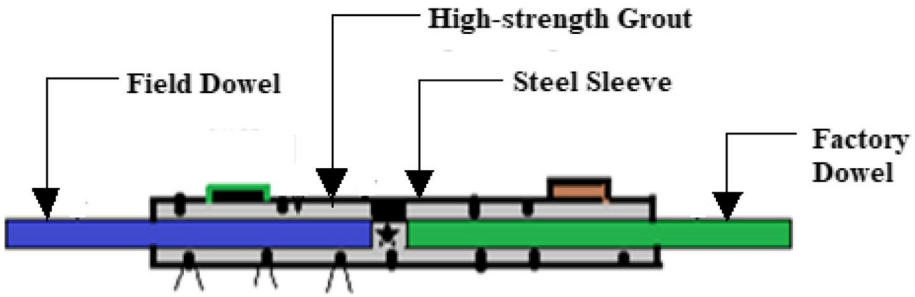

Fig. 7 Grouted Splice-Sleeve

Table 3 Design axial load of RC pier

f'_c (ksi) (MPa)	f_y (ksi) (MPa)	A_g (sq-in) (sq-cm)	A_{st} (sq-in) (sq-cm)	A_{net} (sq-in) (sq-cm)	$A_{core,net}$ (sq.in) (sq-cm)
3 (20.68)	60 (413.68)	346.361 (2234.58)	4.74 (30.58)	341.621 (2204.00)	341.621 (2204.00)

5.1 Computation of bending stresses at column base

In order to estimate the bending stresses occurring at the column base due to the unbalanced moment from the impact, some geometric properties of the column such as the distance of the extreme fiber from the neutral axis (NA) as well as the moment of inertia need to be evaluated. Determination of bending (flexural) stresses (σ_b) experienced by the pier is as shown in Eq. 20 (Ameli and Pantelides 2017).

$$\sigma_b = M_{un} * \left(\frac{c}{I_{avg}}\right) \tag{20}$$

Where: M_{un} represents the unbalanced moments for static, dynamic and for both gross and core cross-sectional areas (Fig. 4). '*c*' represents the distance of the extreme fiber from in the neutral axis (as shown in Fig. 3), and I_{avg}, is the average moment of inertia of the column cross section.

5.2 Determination of direct stresses

Direct stress (σ_o) and design axial compressive load the pier undertaken have been computed from the Eq. 21 (Ameli and Pantelides 2017) and 22 (MacGregor et al. 2012), respectively.

$$\sigma_o = \frac{P_n}{A_g} \tag{21}$$

$$P_n = 0.85 f'_c \left(A_g - A_{st}\right) + A_{st}\sigma_y \tag{22}$$

Where: f'_c is the 28-day concrete compressive strength, A_g is the gross cross-sectional area, A_{st} is the area of 6 # 8 (1 in. or 25.4 mm diameter) reinforcing bars, and σ_y is the yield strength of the reinforcing steel re-bar.

Table 4 Direct stresses for gross and core cross-sections

P_n (kips) (kN)	P_a (kips) (kN)	$\sigma_{0,gn}$ (kip/sq.in) (kN/cm^2)	$\sigma_{0,cn}$ (kip/sq.in) (kN/cm^2)
687.54 (3058.33)	687.54 (3058.33)	1.98504584 (1.3686)	2.012588401 (1.3876)

Details of the necessary input data for the stress computations are tabulated in Table 3, and the resulting stresses in Table 4.

5.3 Determination of combined stresses governed by grouted coupler

The stress experienced by each coupler (σ) is expressed as the sum of direct stress (σ_o) and bending stress (σ_b) (Girão Coelho et al. 2012). Known as combined stress, this summation of stresses is computed as shown in Eq. 23.

$$\sigma = \sigma_o \pm \sigma_b \tag{23}$$

Where: σ_o and σ_b represent direct and bending stress respectively.

In Eq. 25, (+) and (−) signs indicate tensile and compressive stresses, respectively.

To analyze the response of the reinforced concrete pier to external impact events, two scenarios are studied. These are the effect of impact at different heights on the resulting moments and stresses at the base of the column as well as the resulting moments and stresses at different points of the pier from impact at a particular point.

5.3.1 Case – I Impact at different heights

Computation of combined stresses at the base in the column for single coupler caused by the impacts in column are shown in Fig. 7. Different impact heights are considered as the frontal height of the semi-trailer is approximately 3 ft. (1 m). Maximum height of impact is taken as 4.029 ft. (1.5 m) to account for possible elevation of the semi-trailer bouncing off a bumper just prior to impact. For each single vehicular hit, combined stresses (both tensile and compressive) experienced by the column and by extension each coupler are shown in Fig. 8.

From the Fig. 9, it can be deduced that there is a linear trend in the stresses with a change in height of impact location. The stresses at the base increase as the height of the impact location increases. This can be attributed to the increase in the moment generated at the base with an increase in the distance of the impact from the base. Also, there is very little difference in the stresses occurring in the gross and core areas. This means that the concrete cover adds only a very limited capacity to the overall capacity of the column. However, there is a distinct change in the resulting stresses when the effect of strain rate is included using the DIF. The resulting stresses (labeled as dynamic stresses) are significantly larger than those from a static loading scenario, indicating that the use of static forces without adequately compensating for the dynamic nature of the impact loads will lead to overly liberal estimates of the stresses.

5.3.2 Case – II Stresses at different heights from impact at a single location

Combined stresses at different fiber levels from impact at a constant height of 3 ft is as shown in Fig. 9. Direct stress from induced from axially compression load and flexural

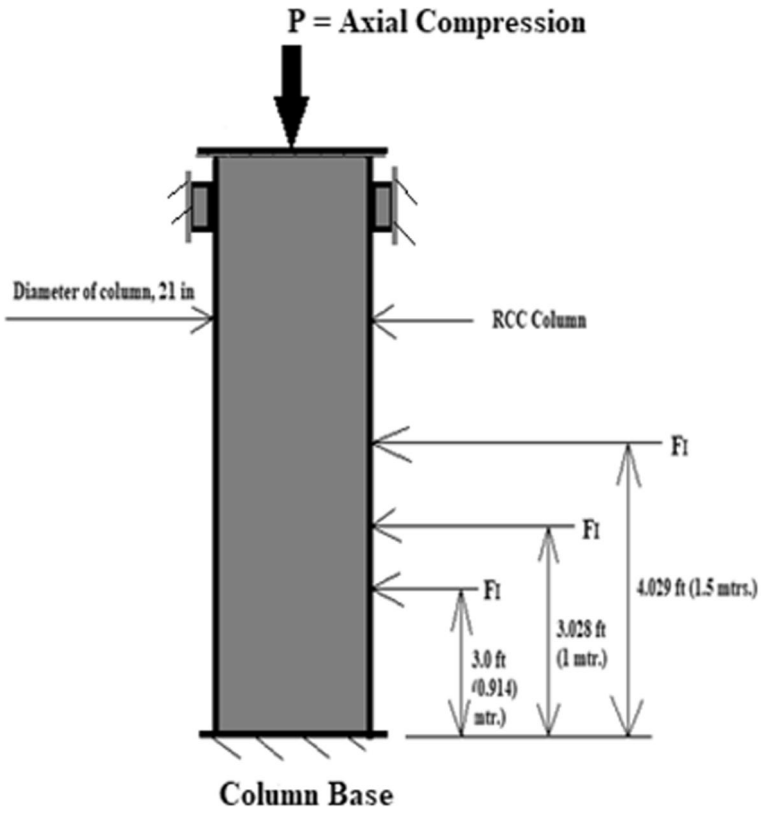

Fig. 8 Vehicular strike in column at different levels

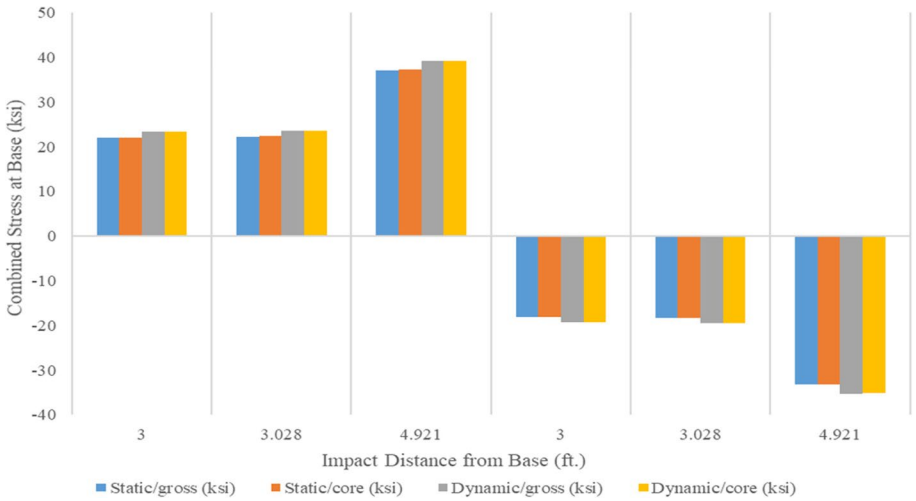

Fig. 9 Combined stresses in column base experienced by single coupler

stress from bending caused due to impact are summed up to compute the resultant combined stresses for both static and dynamic are as shown in Figs. 10 and 11.

From the results, it can be observed that although the maximum balanced moments, and by extension the maximum combined stresses, occur at the base of the

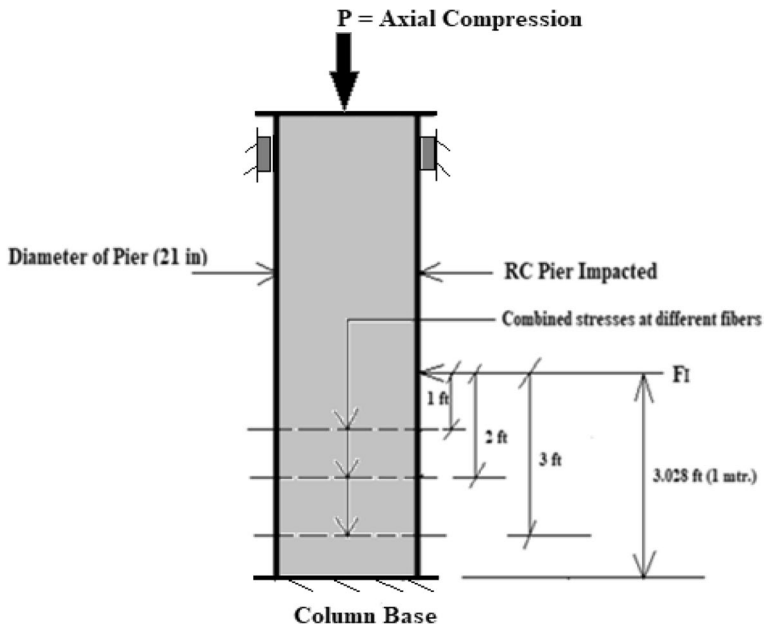

Fig. 10 Stresses in column at different fiber levels

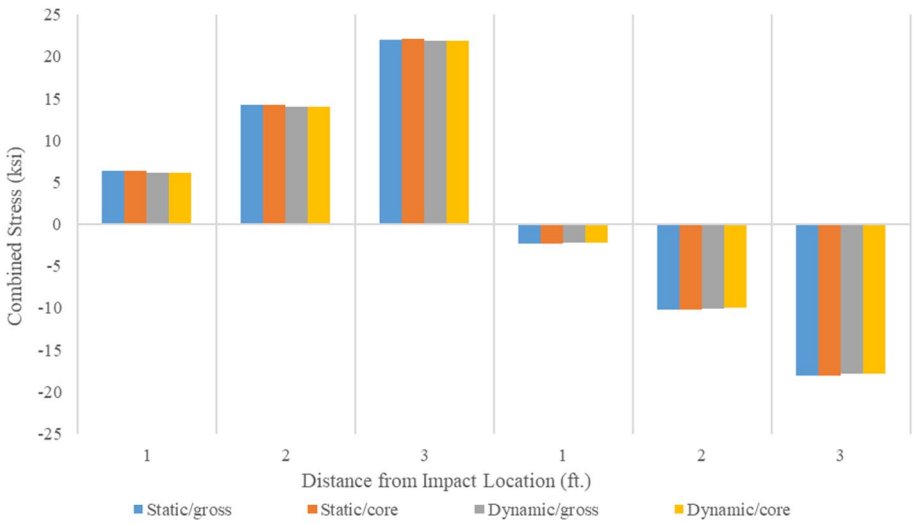

Fig. 11 Combined stresses in column at different fiber level

column (i.e. at the maximum distance from the point of impact), moment overpressures also occur at other sections of the column. These moment overpressures result in combined stresses exceeding the capacity of the pier. This implies that although the use of couplers in the base of the pier may improve its stiffness and thus its resistance to unbalanced moments at the base, the column will still possibly fail at other locations away from the base where the coupler has no significant effect. As a result, in addition to the use of couplers, other measures need to be adopted to improve the moment capacity of the pier and prevent collapse.

6 Finite element model (FEM) of the grouted coupler

To corroborate the results obtained from the analytical analyses carried out, a composite finite element model (FEM) consisting of concrete cylinder (3 ksi or 20.68 MPa), cast iron hollow cylindrical splice- sleeve, concrete grout (6 ksi or 41.36 MPa), and single reinforcing steel reinforcing bar are designed and analyzed using the commercial software ANSYS Mechanical. This model is designed to characterize a single coupler unit with concrete cover. Hollow cylindrical cast iron splice-sleeve (36 ksi or 248 MPa)) is used along steel rebar (60 ksi or 413 MPa) embedded in the splice sleeve. Figure 12 shows the designed finite element model (FEM) of the grouted coupler. For all three different materials and their attachments, non-separable contacts have been considered to act as a monolithic behavior of the model under vertical axial compression and horizontal impact. During simulation, high frictions are developed at the contacts of all inter-material surfaces. The coupler-rebar model considered in this study shows large deformation as a result of transmitting horizontal load while the RC bridge pier experiences vehicle impact. Material properties utilized for developing the numerical model are shown in Table 5.

A rectangular mesh is applied to the model resulting in 7080 elements. Figure 13 shows the resulting meshed model.

Axial load from the superstructure is scaled down with respect to the cross-sectional area of the model. The load from impact is applied in a similar version albeit as a moment occurring at the base of the column.

7 Results from FEM

Analyses of the model under both static and dynamic loading conditions are performed. Results from these analyses are presented in this section.

7.1 Stress concentration in coupler

Figures 14 and 15 show the resulting combined axial and bending stresses from the static and dynamic loading conditions respectively. The results show an agreement

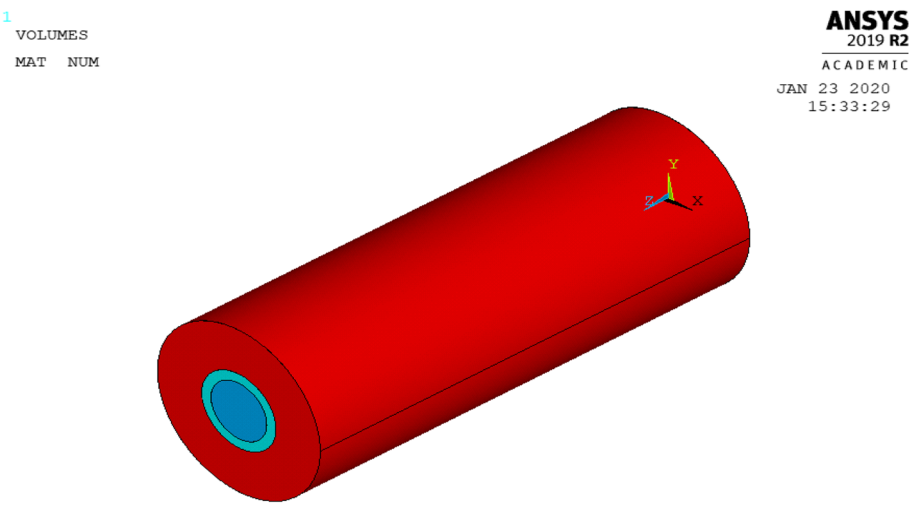

Fig. 12 Finite element model of grouted coupler and cover concrete

Table 5 Material Properties for Finite Element Model (FEM)

Materials	Material properties and respective values	
Cast Iron	Modulus of Elasticity (psi) (MPa)	$1.29*10^7$ ($8.9*10^4$)
	Poisson's Ratio	0.3
	Cast-Iron with Isotropic Hardening	0.04
Reinforcing Steel	Modulus of Elasticity (psi) (MPa)	$2.9*10^7$ ($1.9*10^5$)
	Poisson's Ratio	0.3
	Yield Stress (psi) (MPa)	60,000 (413.68)
	Tangent Modulus (psi) (MPa)	2900 (19.995)
Concrete	Modulus of Elasticity (psi) (MPa)	$3.6*10^6$ ($2.48*10^4$)
	Poisson's Ratio	0.18
	Open Shear Transfer Coefficient	0.3
	Closed Shear Transfer Coefficient	1
	Uniaxial Cracking Stress (psi) (MPa)	474.34 (3.27)
	Uniaxial Crushing Stress (psi) (MPa)	−1 (− 0.0069)
Concrete Grout	Modulus of Elasticity (psi) (MPa)	$4.415*10^6$ ($3.04*10^4$)
	Poisson's Ratio	0.2
	Open Shear Transfer Coefficient	0.3
	Closed Shear Transfer Coefficient	1
	Uniaxial Cracking Stress (psi) (MPa)	750 (5.17)
	Uniaxial Crushing Stress (psi) (MPa)	-1 (−0.0069)

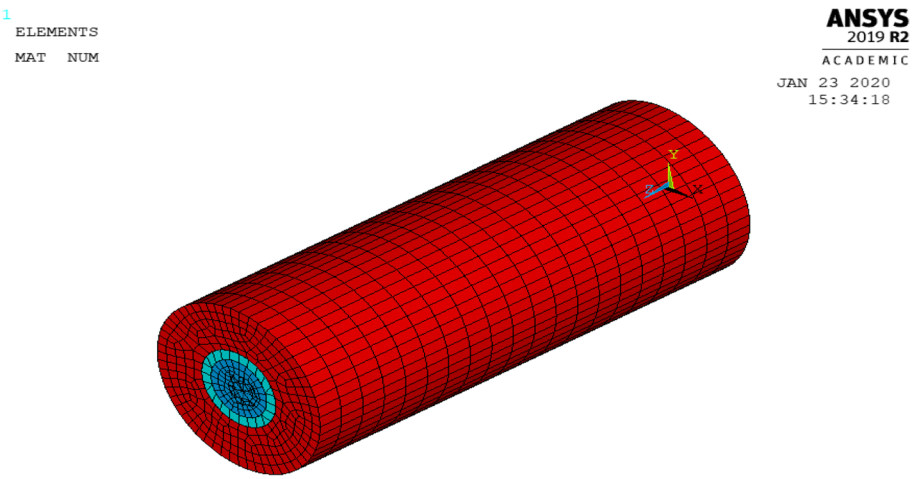

Fig. 13 Meshed model

in the values of maximum stresses obtained from the calculations. The maximum stresses from the finite element analyses are slightly higher than the those obtained from corresponding stress calculations. This can be attributed to an increased precision expected of finite element analysis in comparison to less complicated computation methods.

Figures 14b and 15b show stress concentration from the applied loads within the grouted coupler. This indicates that the coupler system bears the brunt of the unbalanced moment resulting from the impact scenario. This leads to an extensive crack system developing in the concrete grout inside the splice sleeve. Figures 16 and 17 show these crack patterns.

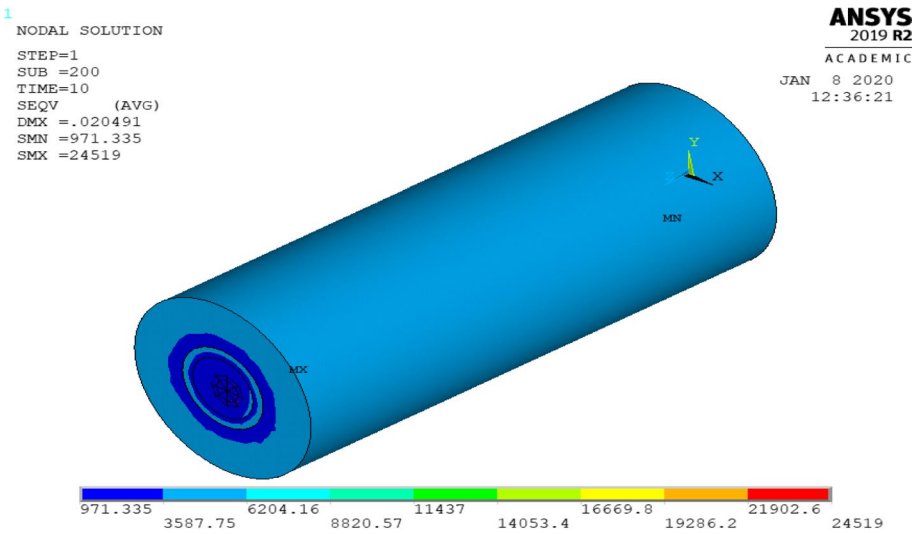

(a)

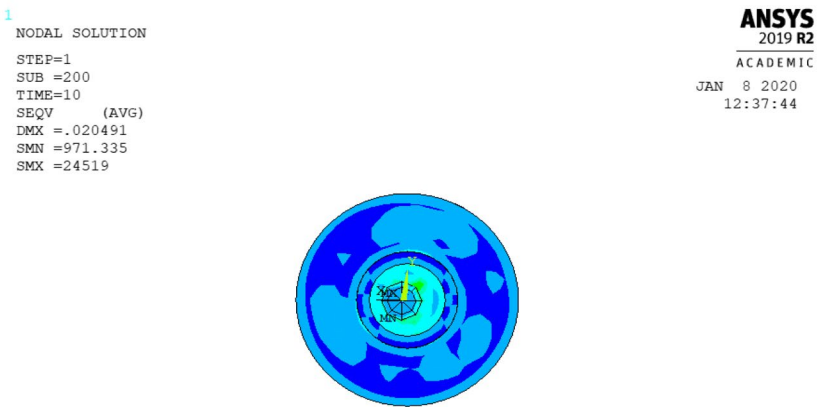

(b)

Fig. 14 **a** Combined stresses from static model. **b** Combined stresses from static model

From Figs. 16 and 17, it can be deduced that in resisting most of the unbalanced moment, the coupler system ensures the concrete column retains its serviceability. The crack pattern shows that all resulting cracks from the loading developed in the concrete grout, limiting damage to the column in just the coupler system, and leaving the surrounding concrete intact and thus serviceable.

7.2 Strain in coupler

Figure 18 shows the strain developed in the coupler in the finite element model. This coupler model, corresponding to a length ratio of 1 (only a section of the column corresponding to the length of the coupler was modeled), with a rigid length factor of 0.65 (from the proposed value for grouted couplers in (Tazarv and Saiidi 2016)).

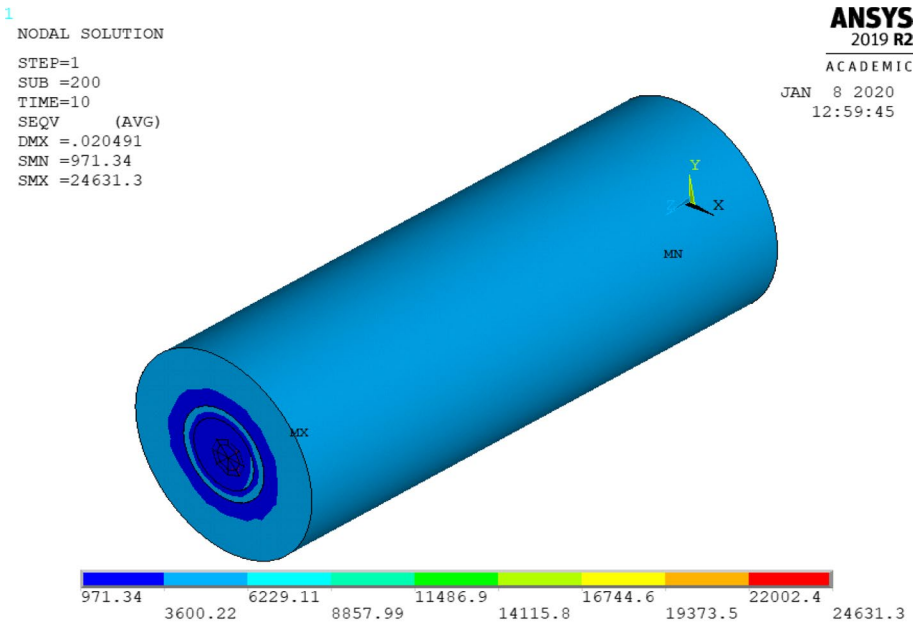

(a)

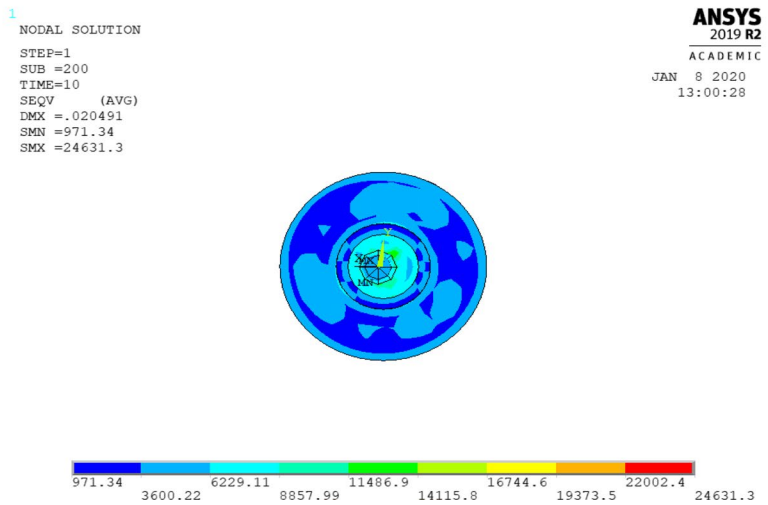

(b)

Fig. 15 **a** Combined stresses from dynamic model. **b** Combined stresses from dynamic model

8 Uniaxial stress-strain concentration model for coupler

Spliced bars used as grouted couplers exhibit different behavior to reinforcing steel reinforcing bars due to the anchoring mechanism (bond behavior of coupler system with reinforcement) (Tazarv and Saiidi 2016). The anchoring mechanism for the spliced bar manifests a rigid body behavior depending on the stress-strain relationship and the stress concentration at the coupler region ($L_{critical}$). To determine the stress-strain relationship of the coupler region some physical properties of the coupler system, including the coupler rigid length factor (β) and its length play a significant role.

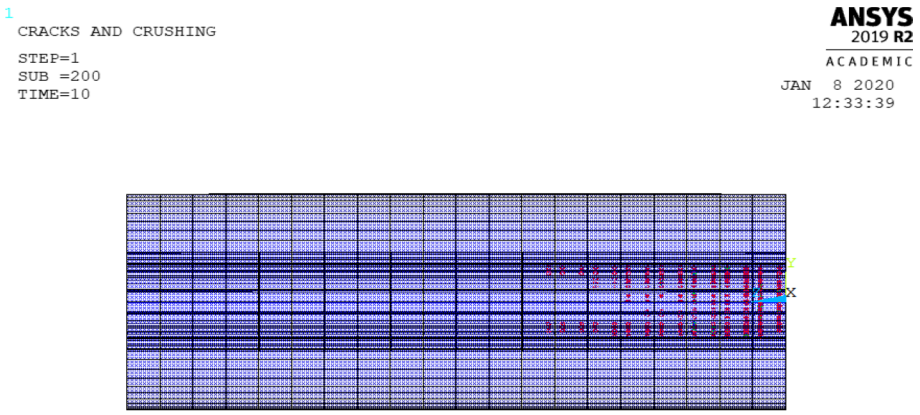

(a)

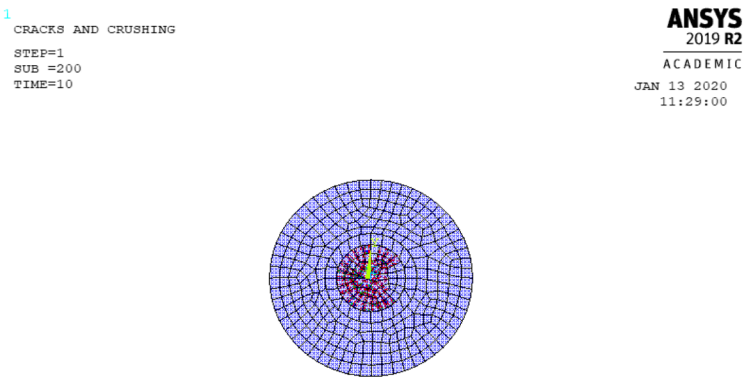

(b)

Fig. 16 **a** Crack pattern in model for static loading. **b** Crack pattern in model for static loading

Under tension, only a part of the coupler system will undergo elongation. A section in the middle will stay rigid due to larger diameter of the coupler relative to the reinforcing steel as well as its anchoring mechanism (Tazarv and Saiidi 2016). This rigid length can be determined using a coupler rigid length factor (β) which is a function of the coupler type. This factor has been experimentally determined for different coupler types in (Tazarv and Saiidi 2016). Strain in the coupler can be computed using the relationship in Eq. 24 (Tazarv and Saiidi 2016).

$$\varepsilon_{sp}/\varepsilon_y = \left(L_{critical} - \beta.L_{sp}\right)/L_{critical} \tag{24}$$

Where: ε_{sp} is the required strain at the coupler region, ε_y is the strain at the connecting steel re-bar, L_{sp} is the coupler length, $L_{critical}$ is the coupler region length, and b is the coupler rigid length factor.

Figure 19 shows the geometry of the coupler system with some of its physical dimensions, which are used in Eq. 24.

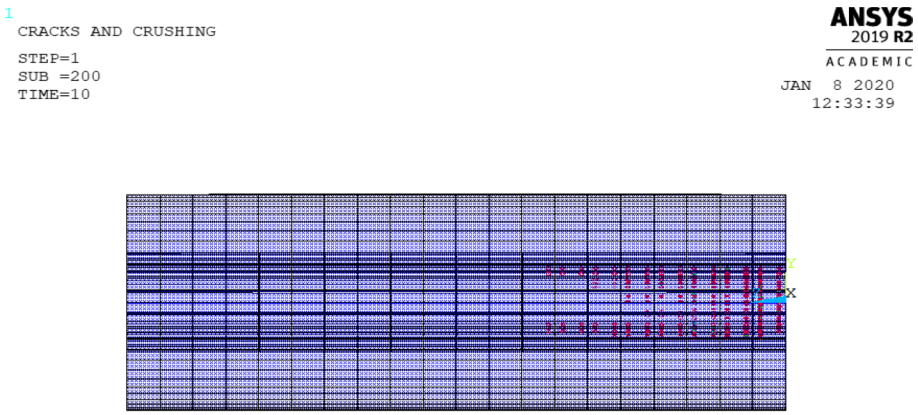

(a)

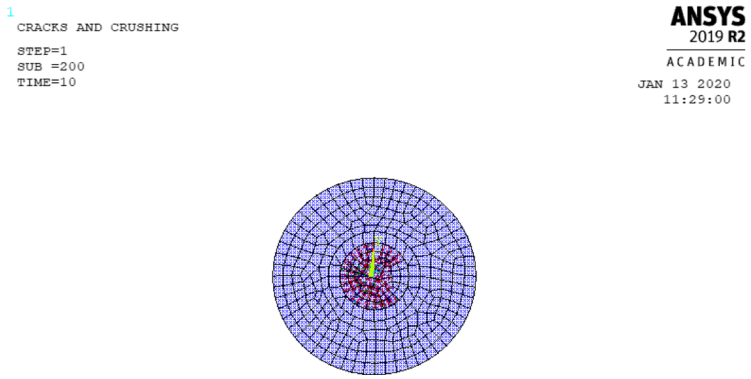

(b)

Fig. 17 **a** Crack pattern in model for dynamic loading. **b** Crack pattern in model for dynamic loading

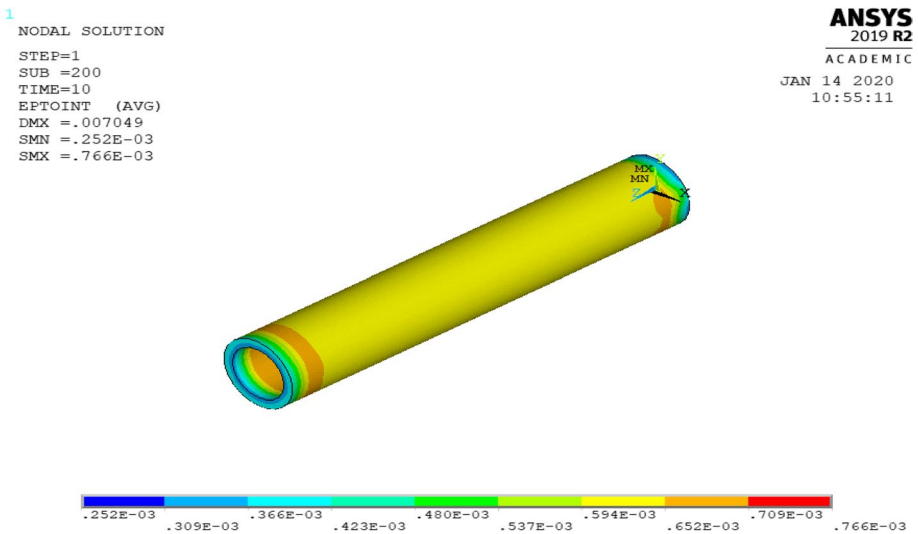

Fig. 18 Maximum strain at coupler edge from dynamic loading

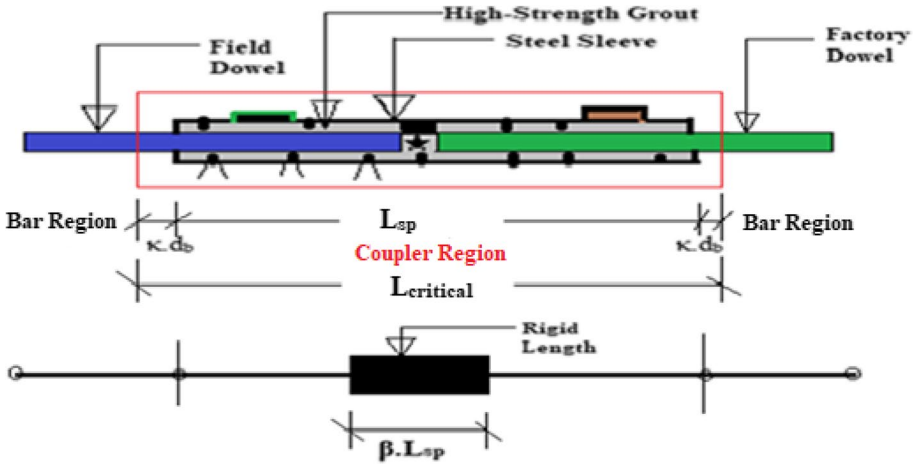

Fig. 19 Uniaxial stress-strain concentration in coupler

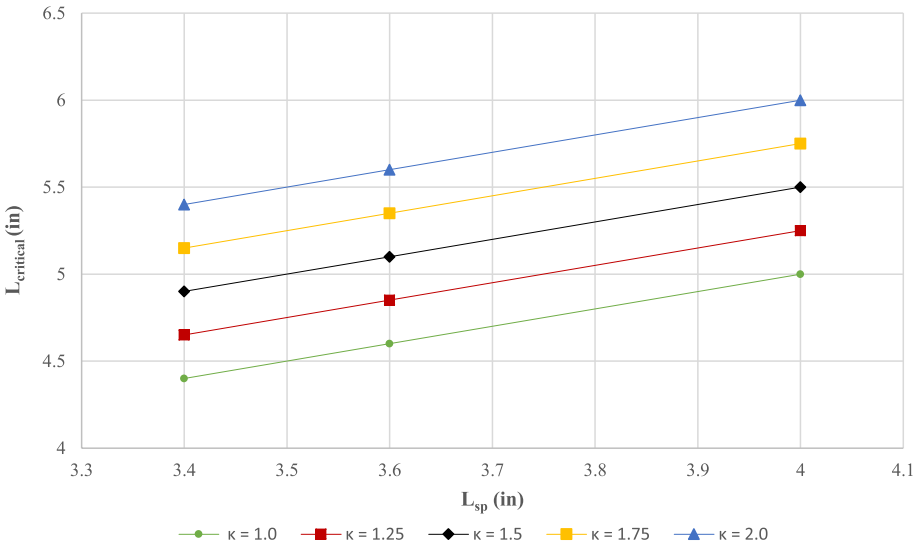

Fig. 20 L_{sp} with the corresponding $L_{critical}$ and at various κ (1 to 2)

The coupler region extends beyond each side of the coupler sleeve length (L_{sp}), by a factor defined by the diameter of reinforcing steel (d_b) due to its having a higher stiffness than the adjacent steel rebar as shown in Fig. 18 (Haber et al. 2014). The coupler critical length ($L_{critical}$) can be computed using its physical length (L_{sp}) and the diameter of the reinforcing steel as shown in Eq. 25 (Tazarv and Saiidi 2016).

$$L_{critical} = L_{sp} + 2\kappa d_b \tag{25}$$

Where: d_b is the diameter of reinforcing steel re-bar, L_{sp} is the coupler sleeve length, $L_{critical}$ is the coupler critical length, and κ is the factor varies from 1.0 to 2.0 (Ameli and Pantelides 2017).

In order to determine the influence area of the highly stressed zone induced by impact, $L_{critical}$ has been given substantial importance, and needs to be computed. The length $L_{critical}$ is actually extended beyond the splice-sleeve zone and some portions of the steel

rebar extended from both the sides are considered as shown in Fig. 19. To understand the deformations at steel rebar and splice-sleeve junction, κ plays a very sensitive role for the computation of the highly stressed zone, the critical length ($L_{critical}$) of the coupler.

Figure 20 shows the linear relationship used to identify $L_{critical}$ from the defined coupler sleeve length (L_{sp}). In order to determine $L_{critical}$ from the specified L_{sp} carried out from the conservative κ values ranging from 1.0 to 2.0 (Ameli and Pantelides 2017), χ, the ratio of coupler length (L_{sp}) over the coupler region length ($L_{critical}$), can be computed using Eq. 25 and Fig. 18. L_{sp} data can be taken from the splice sleeve specification (ICC-ES Evaluation Report ESR-3433 2014). In this χ is very significant to compute ε_{sp} as mentioned in Eq. 27. Figure 18 shows the relationship between $L_{critical}$ and L_{sp} to in order to establish a holistic methodology for the different κ factors ranging from 1.0 to 2.0. This method includes coupler length (L_{sp}) to determine maximum strain developed at the coupler and steel rebar region while experiencing vehicle impact. In order to ascertaining static strain (ε_{sp}) at coupler region, β and χ play an important role for the chronological computation of ε_{sp}, which are shown in Eqs. 26 and 27.

Modification and rearrangement of Eqs. 24 and 25, yields Eq. 26.

$$\frac{\varepsilon_{sp}}{\varepsilon_y} = 1 - \beta * \chi \tag{26}$$

In Eq. 26, χ, the ratio of coupler length over the coupler region length ($L_{sp}/L_{critical}$), β is the coupler rigid length factor (varies from 0.0 to 1.0) are introduced to predict coupler region induced strain (ε_{sp}). Furthermore, to predict the strain at coupler region, ε_{sp} can be determined from Eq. 27 after re-arranging the Eq. 26.

$$\varepsilon_{sp} = (1 - \beta * \chi) * \varepsilon_y \tag{27}$$

From Eq. 27, it can be deduced that the strain in the coupler system is a function of its geometric parameters as well as the strain induced in the reinforcing steel. As a result, the performance of the coupler system can be designed to meet desired specifications by modifying some of the geometric parameters of the coupler.

From Eq. 26, coupler strain (ε_{sp}) is a function of the mechanical properties of the coupler, including its rigid length factor and its region length.

A maximum strain of 0.00076 is developed in the coupler from the simulated impact occurring on the concrete pier. This is identical to the expected value of 0.00073 computed using Eq. 27, indicating that the equation provides a good estimate of the relationship between a coupler's mechanical properties and the strain expected to occur in it from external loads.

Considering the modulus of steel reinforcement (E_s) as $29*10^6$ psi, and yield stress of steel re-bar (σ_y) as 60 ksi, the strain in the steel rebar (ε_y) is computed using Hooke's law as 0.0021. The relationship between the mechanical properties of the coupler and the resulting strain is shown in Fig. 21. This figure plots the expected coupler strain for various coupler types (identified by the different rigid length factors β) at different length ratios (χ).

Coupler strains (ε_{sp}) for different coupler length ratio (χ) ranging from 0.625 to 0.80 and at the corresponding κ values (ranging between 1.0 and 2.0) are computed for steel strain of 0.0021. These plots allow for an estimation of the strain that will be developed

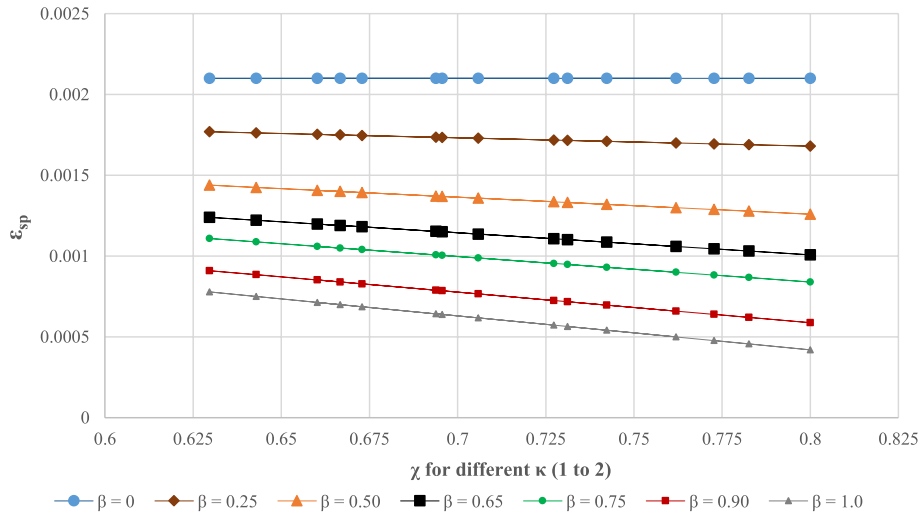

Fig. 21 Evaluation of ε_{sp} and χ for corresponding κ at ε_y of 0.0021

in a coupler system with respect to its mechanical properties. Each plot represents a specific coupler rigid length factor (β), which is a function of the coupler type. Respective coupler strains are computed for β ranging between 0 to 1, and as shown in Fig. 21. The plots show a linear relationship between the coupler strain and its length ratio. This relationship is more evident at higher β values and trends towards a uniform strain value at the β of zero. This indicates that the material and geometrical properties of the coupler play an important role in its strain capacity, helping in designing coupler systems to meet specific service demands.

8.1 Determination of strain-rate at coupler region

During dynamic impact, the strain rate in the critical region ($L_{critical}$) changes linearly with changes in the strain rate of the steel rebar connected to the coupler. Strain rates of the steel rebars due to vehicle impact on a circular RC bridge pier are estimated to range between 10^{-1} and 10^{-4} for quasi-static to dynamic state at a yield stress of 60 ksi (Malvar and Crawford 1998). Dynamic strain rates in the coupler region can be assessed by partial derivative of Eq. 27 with respect to time (t) in seconds. This yields Eq. 28 which can be used to predict strain rates in the coupler region. Steel rebar strain rate ($\delta\varepsilon_y/\delta t$) and strain rate at coupler ($\delta\varepsilon_{sp}/\delta t$) are expressed as $\acute{\varepsilon}_y$ at yield as $\acute{\varepsilon}_{sp}$ in Eq. 28.

$$\acute{\varepsilon}_{sp} = (1 - \beta * \chi) * \acute{\varepsilon}_y \tag{28}$$

Where: The variables $\acute{\varepsilon}_y, \acute{\varepsilon}_{sp}, \beta$, and χ are already explained.

Simulations of the expected coupler strain rates ($\acute{\varepsilon}_{sp}$) at different coupler length ratios (χ) and for the different steel rebar strain rates are investigated. This could feasibly occur during the impact events are undertaken to gain an insight into the behavior of the coupler at changing strain rates in steel rebar. Shown in the Figs. 22, 23 and 24 are the respective different steel rebar strain rates of 10^{-1} sec, 10^{-2} sec, 10^{-3} sec, and 10^{-4} sec, for increasing χ values at the specified coupler strain rates depending on various κ factors ranging from 1 to 2.

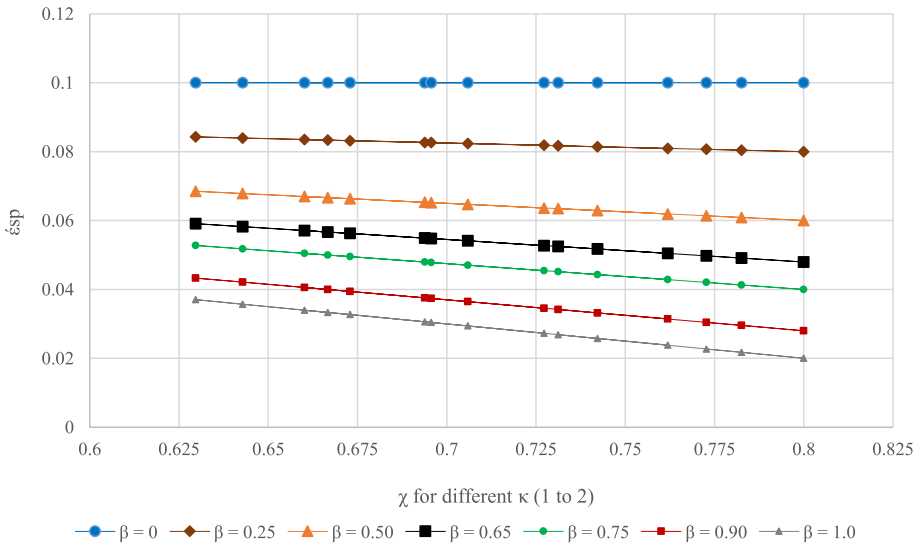

Fig. 22 $\acute{\varepsilon}_{sp}$ and χ for corresponding κ at $\acute{\varepsilon}_{y}$ of 0.1

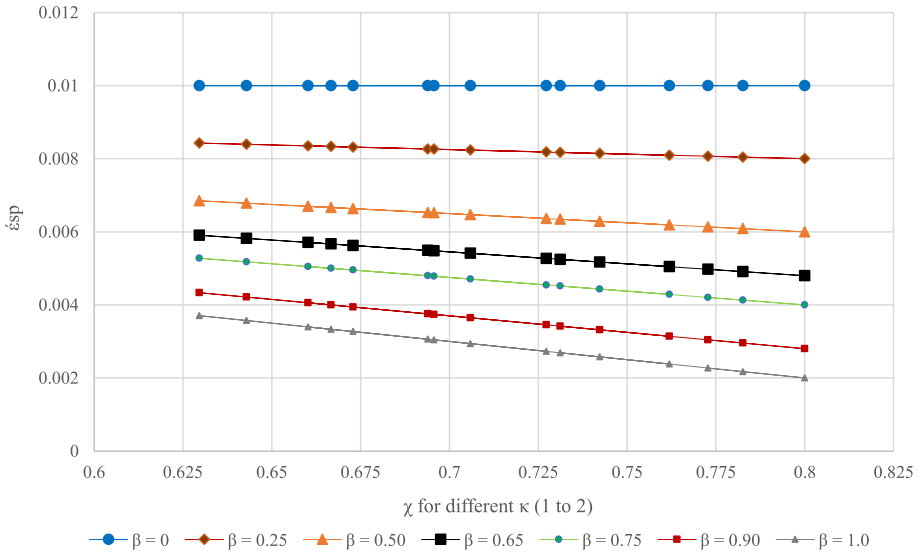

Fig. 23 $\acute{\varepsilon}_{sp}$ and χ for corresponding κ at $\acute{\varepsilon}_{y}$ of 0.01

Figures 22, 23, 24 and 25 show the different strain rates expected in the coupler region from various impact conditions at different coupler length ratios (χ) and at different possible steel rebar strain rates ($\acute{\varepsilon}_{y}$). Coupler region strain rates ($\acute{\varepsilon}_{sp}$) show the linear trends with respect to the χ values, indicating an increase in the expected strain rate in the coupler region with a reduction in its critical length. As such, for the known strain rates in steel, which is a function of loading, the corresponding coupler strain rates can be easily determined.

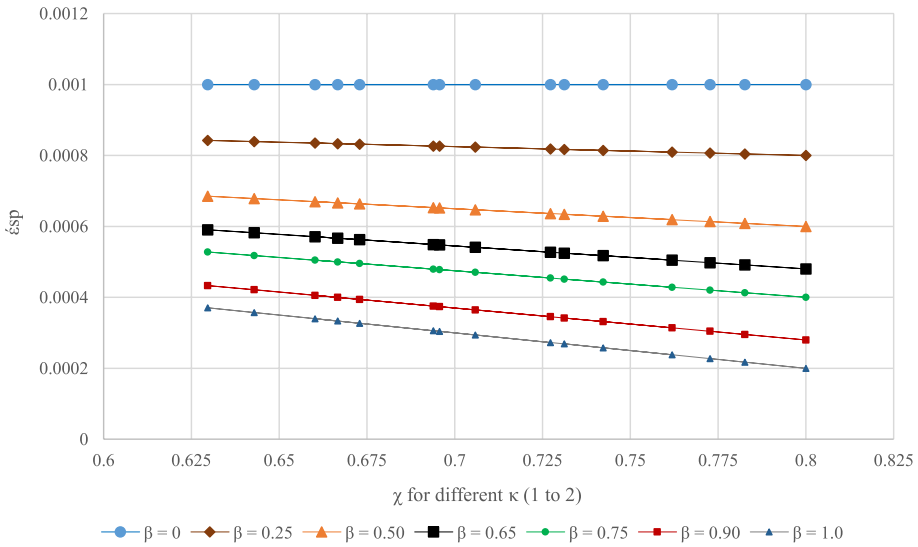

Fig. 24 $\acute{\varepsilon}_{sp}$ and χ for corresponding κ at $\acute{\varepsilon}_{y}$ of 0.001

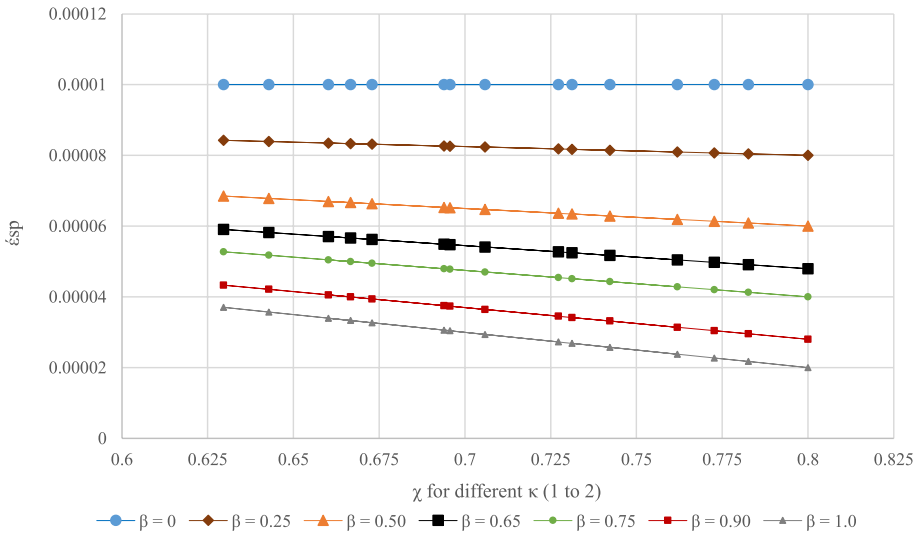

Fig. 25 $\acute{\varepsilon}_{sp}$ and χ for corresponding κ at $\acute{\varepsilon}_{y}$ of 0.0001

9 Discussions and conclusions

In reinforced concrete (RC) structures, piers are usually the most vulnerable members to collisions due to its exposed face and slender behavior. In particular, the desired characteristics and the associated impact performance levels of the critical components warrant additional investigation. The following observations and conclusions are drawn from this study:

- In this research, a means of addressing a critical component of the pier behavior during a vehicular impact scenario is investigated. This involves the use of a grouted coupler connection system to improve stiffness, and thus increase the moment capacity of the pier and by extension reduce the risk of collapse of the pier from unbalanced moments expected to occur during impact. Combined stresses in the base and at different fiber sections as a result of vehicular impact in the pier are analyzed, and the results are shown

for both bending compression and bending tension. A finite element model (FEM) is also used to corroborate the computed stresses expected to occur from vehicle impact at the base of the pier, as well as to investigate the benefit of including a grouted coupler sleeve at this vulnerable spot to limit the damage taking place during impact. The investigations reveal that the grouted coupler performs quite well in containing the unbalanced moments from the impact, without cracking the concrete of the pier footing, while observing cracks in the grout for both static and dynamic impact loads.

- Further investigations into the strain rate developed in the coupler during impact provide an insightful notion in establishing and understanding the relationship between strain and mechanical properties of the coupler at impact load. This relationship ensures that couplers going forward can be designed to adequately compensate for loading scenarios resulting in moments, exceeding the design capacity of the reinforced concrete (RC) bridge piers, and thus save them from excessive damage. Beyond the investigations carried out in this study, it is also imperative to investigate the behavior of grouted couplers in other positions besides being embedded in the foundation. Also, other possible materials for the coupler sleeve besides cast iron as well as some other grout mixes (with higher compressive strengths) need to be scrutinized to fully comprehend the influence of the coupler system to a pier's resistance in counteracting impact loads.
- This study is an attempt to determine the dynamic strain comprising the model during and post impact scenario. Maximum strain can be found at $\beta = 0$, which corresponds to having no coupler and the entire strain developed is totally induced in the steel rebar. The strain rate is particularly useful for very short impact durations where instantaneous strain is impossible to determine.

The methods utilized in this study can also help improve design, providing designers with information on how the grouted couplers can be expected to behave under lateral impact loads. However, further experimental studies involving various pier geometries, different material properties, and changing the coupler's position are warranted to investigate and capture the performance under various impact scenarios.

Table 6 Conversion chart for the US customary to the equivalent SI units

US Customary	SI Unit
1 ksi	6.89 MPa (kN/mm^2)
1 ksi	6894.76 kN/m^2
1 kip-in	0.113 kN-m
1 kip	4.45 kN
1 lbs	0.00445 kN
1 mph	1.61 km/hr
1 ft lb./sec	0.00136 kN-m/sec (1.36 N-m/sec)
1 in	0.0254 m (25.4 mm)
1 ft	0.3048 m (304.80 mm)
1 pci	271.4471 kN/m^3
1 psi	6.8947 kN/m^2

Appendix

Table 6

Abbreviations

M_n	Nominal moment strength
E_s	Modulus of elasticity of steel
E_c	Modulus of elasticity of concrete
f'_c	Compressive strength of concrete
f_y	Yield strength of steel
ε_y	Strain at steel corresponding to f_y
c	Height of compression block
n	Modular ratio
β_1	Ratio of depth of rectangular stress block to the depth to the neutral axis
h	External diameter of the concrete column
d_t	Distance from extreme compression fiber to extreme tension steel
x_b	Distance from the extreme compression fiber to the neutral axis for a balanced strain condition
a_b	Depth of Whitney equivalent rectangular stress distribution in concrete for a balanced strain condition
α	Angle between two rebar's at center of the circular area
A_{cb}	Area of circular compression block
$\overline{X}$	Centroid location of circular compression block
C_c	Compressive force in concrete for circular compression block
C_s	Compressive force in longitudinal reinforcement
T	Tensile force of steel
P_n	Nominal axial compressive strength
P_a	Axial compressive strength
$M_{n,g}$	Nominal moment capacity for the gross concrete area of the column
h_c	Diameter of the core concrete
A_{gc}	Gross area of the core concrete
A_{nc}	Net area of the core concrete
A_c	Area of the core concrete
A_g	Gross cross-sectional area
$C_{c,c}$	Compressive for of the core concrete
$P_{n,c}$	Nominal axial compressive strength of the core concrete
$M_{n,c}$	Nominal flexural capacity for the core concrete section
σ_{dyn}	Dynamic flow stress
$\acute{\varepsilon}$	Quasi-static strain rate of steel re-bar
$\acute{\varepsilon}_y$	Quasi-static strain rate at steel re-bar
$\acute{\varepsilon}_{sp}$	Strain rate at coupler
σ_y	Static flow stress
$\bar{\sigma}_{dyn}$	Dynamic flow stress in steel during impact
ξ	Dynamic parameter
DIF	Dynamic increase factor
I_{dyn}	Frontal shock due to impact
I_r	Peak reflected pressure (overpressure)
t_d^+	Time instant of the peak impact force
t	Impact duration
V	Maximum permissible velocity
M_s	Static moment
t	Time of collision
H	Height of collision
M_{dyn}	Dynamic moment
$M_{un,sg}$	Unbalanced moment for static gross cross-sectional area
$M_{s,g}$	Static moment at gross concrete area
$M_{n,g}$	Nominal moment capacity for gross concrete area
$M_{un,sc}$	Static unbalanced moment for core cross-sectional area
$M_{un,dg}$	Dynamic unbalanced moment for core cross-sectional area
$M_{dyn,g}$	Dynamic moment at gross concrete area
$M_{un,dc}$	Dynamic unbalanced moment for core cross-sectional area
σ_b	Bending stress
σ_o	Direct stress
I_{avg}	Average moment of inertia of each splice sleeve
c	Distance of the extreme fiber from the centroid
P	Axial compressive force
σ	Combined stress
W	Wider end of the splice sleeve
N	Narrower end of the splice sleeve
χ	Coupler length ratio (L_{sp} / L_{cr})
β	Coupler rigid length factor
L_{sp}	Coupler length

$L_{critical}$ Coupler region length
κ A factor ranges from 1.0 to 2.0

Acknowledgements
This publication was supported by a subcontract from Rutgers University, Center for Advanced Infrastructure and Transportation (CAIT), under DTFH62-08-C-00005 from the U.S. Department of Transportation-Federal Highway Administration (USDOT-FHWA) and NMB Splice-Sleeve. Any opinions, findings, and conclusions or recommendations expressed in this publication are those of the author(s) and do not necessarily reflect the views of Rutgers University and NMB Splice-Sleeve or those of the U.S. Department of Transportation-Federal Highway Administration.

Authors' contributions
Suman Roy*[1]: Conceptualized and developed the theoretical formalism, numerical models (FEM) and simulations, validation, performed the analytic calculations, and writing draft. Ikwulono D. Unobe[1]: Apprehended the analytic calculations, performed the numerical simulations, and edited the draft. Andrew D. Sorensen[1]: Conceptualized and overall guidance, editing manuscript and supervised the project. The authors have read and approved the final manuscript.

Funding
1) Center for Advanced Infrastructure and Transportation (CAIT), under DTFH62-08-C-00005 from the U.S. Department of Transportation-Federal Highway Administration (USDOT-FHWA).
2) NMB Splice-Sleeve – North America, USA.

Availability of data and materials
Some or all data, models, or code that support the findings of this study are available from the corresponding author upon reasonable request.

Declarations

Competing interests
We, the authors of the manuscript declare that we have no competing interests.

Received: 1 August 2022 Accepted: 12 September 2022
Published online: 04 November 2022

References

ACI (2011) ACI 318-11: building code requirements for structural concrete. American Concrete Institute, United States of America
Ameli MJ, Brown DN, Parks JE, Pantelides CP (2016) Seismic column-to-footing connections using grouted splice sleeves. ACI Struct J 113(5):1021–1030 American Concrete Institute
Ameli MJ, Pantelides CP (2017) Seismic analysis of precast concrete bridge columns connected with grouted splice sleeve connectors. J Struct Eng 143(2):4016176 American Society of Civil Engineers
ASTM (2015) A706/A706M — 15 standard specification for low-alloy steel deformed and plain bars for concrete. ASTM International, United States of America, pp 1–6
Auyeung S, Alipour A, Saini D (2019) Performance-based design of bridge piers under vehicle collision. Eng Struct 191:752–765 Elsevier
Cao R, Agrawal AK, El-Tawil S, Xu X, Wong W (2019) Heavy truck collision with bridge piers: computational simulation study. J Bridge Eng 24(6):4019052 American Society of Civil Engineers
Cowper G, Symonds P (1957) Strain hardening and strain-rate effects in the impact loading of cantilever beam. Brown University Division of Applied Mathematics, United States of America, pp 1–46
Ebrahimpour A, Earles BE, Maskey S, Tangarife M, Sorensen AD (2016) Seismic performance of columns with grouted couplers in Idaho accelerated bridge construction applications. Transportation Dept, Idaho
El-Tawil S, Severino E, Fonseca P (2005) Vehicle collision with bridge piers. J Bridg Eng 10(3):345–353
Feyerabend M (1988) Hard transverse impacts on steel beams and reinforced concrete beams. University of Karlsruhe (TH), Germany
Furlong RW (2014) Design for shear, p 37
Girão Coelho AM, Simão PD, Bijlaard FSK (2012) Guidance for the design of spliced columns. J Struct Eng 138(9):1079–1088 American Society of Civil Engineers
Gomez NL, Alipour A (2014) Study of circular reinforced concrete bridge piers subjected to vehicular collisions. Struct Congress 2014:577–587
Grouted splice sleeve connectors for ABC bridge joints in high-seismic regions – transportation blog (n.d.). https://blog.udot.utah.gov/2014/09/grouted-splice-sleeve-connectors-for-abc-bridge-joints-in-high-seismic-regions/. (Jul. 13, 2020)
Haber ZB, Saiidi MS, Sanders DH (2014) Seismic performance of precast columns with mechanically spliced column-footing connections. ACI Struct J 111(3):639–650 American Concrete Institute
Hsiao JK (2012) Bending-axis effects on load-moment (PM) interaction diagrams for circular concrete columns using a limited number of longitudinal reinforcing bars. Electron J Struct Eng, EJSE International Ltd., University of Melbourne Grattan St. Parkville VIC 12:1
ICC-ES Evaluation Report ESR-3433 (2014). https://icc-es.org/report-listing/esr-3433/
ICC-ES Report (2016). https://icc-es.org/report-listing/esr-3433/
Jacob GC, Fellers JF, Starbuck JM, Simunovic S (2004) Crashworthiness of automotive composite material systems

Karim H, Sheikh MN, Hadi MNS (2014) Confinement of circular concrete columns: a review. In: Proceeding of The 1st International Engineering Conference on Developments in Civil & Computer Engineering Applications (IEC2014), pp 28–36
MacGregor JG, Wight JK, Teng S, Irawan P (2012) Reinforced concrete: mechanics and design. Prentice Hall, Upper Saddle River
Malvar LJ (1998) Review of static and dynamic properties of steel reinforcing bars. ACI Mater J 95(5):609–616
Malvar LJ, Crawford JE (1998) Dynamic increase factors for steel reinforcing bars, 28th DDESB seminar edn, Orlando. https://www.researchgate.net/publication/235099732_Dynamic_Increase_Factors_for_Steel_Reinforcing_Bars
Mander JB, Priestley MJ, Park R (1988) Theoretical stress-strain model for confined concrete. J Struct Eng (United States) 114(8):1804–1826
Mohammed TA, Parvin A (2013) Evaluating damage scale model of concrete materials using test data. Adv Concrete Constr 1(4):289–304 Techno-Press
Pantelides CP, Ameli MJ, Parks JE, Brown DN (2014) Seismic evaluation of grouted splice sleeve connections for precast RC bridge piers in ABC. Utah Department of Transportation, United States of America
Roy S, Sorensen A (2021a) Energy based model of vehicle impacted reinforced bridge piers accounting for concrete contribution to resilience. 18th international probabilistic workshop: IPW 2020. Springer Nature, United States of America, p 301
Roy S, Sorensen A (2021b) A reliability based crack propagation model for reinforced concrete bridge piers subject to vehicle impact. 18th international probabilistic workshop: IPW 2020. Springer Nature, United States of America, p 95
Roy S, Unobe I, Sorensen AD (2021) Vehicle-impact damage of reinforced concrete bridge piers: a state-of-the art review. J Perform Constr Facil 35(5):03121001 American Society of Civil Engineers
Roy S, Unobe ID, Sorensen AD (2022) Reliability assessment and sensitivity analysis of vehicle impacted reinforced concrete circular bridge piers. Structures 37:600–612 Elsevier
Sharma H, Gardoni P, Hurlebaus S (2015) Performance-based probabilistic capacity models and fragility estimates for RC columns subject to vehicle collision. Comput-Aided Civ Infrastruct Eng 30(7):555–569
Speeding & speed limits index & overview (n.d.). https://www.dot.nd.gov/divisions/programming/docs/SpeedLimitGuidelines.pdf. Accessed September 2015
Tazarv M, Saiidi MS (2016) Seismic design of bridge columns incorporating mechanical bar splices in plastic hinge regions. Eng Struct 124:507–520 Elsevier
Thilakarathna HMI, Thambiratnam DP, Dhanasekar M, Perera N (2010) Numerical simulation of axially loaded concrete columns under transverse impact and vulnerability assessment. Int J Impact Eng 37(11):1100–1112 Pergamon
Thomas RJ, Steel K, Sorensen AD (2018) Reliability analysis of circular reinforced concrete columns subject to sequential vehicular impact and blast loading. Eng Struct 168:838–851 Elsevier
Tsang H, Lam NTK (2008) Collapse of reinforced concrete column by vehicle impact. Comput-Aided Civil Infrastruct Eng 23(6):427–436 Wiley Online Library
Zhang G, Chen Z, Lu J, Xu S, Zhou X (2018) Experimental study on the impact properties of concrete bridge pier reinforced with stainless steel rebar. J Test Eval 46(4):1650–1658 ASTM International
Zhou D, Li R (2018) Damage assessment of bridge piers subjected to vehicle collision. Adv Struct Eng 21(15):2270–2281 SAGE Publications Sage UK: London, England
Zhou D, Li R, Wang J, Guo C (2017) Study on impact behavior and impact force of bridge pier subjected to vehicle collision. Shock Vib 2017:1–12

Publisher's Note

Springer Nature remains neutral with regard to jurisdictional claims in published maps and institutional affiliations.

Submit your manuscript to a SpringerOpen journal and benefit from:

- ► Convenient online submission
- ► Rigorous peer review
- ► Open access: articles freely available online
- ► High visibility within the field
- ► Retaining the copyright to your article

Submit your next manuscript at ► springeropen.com